

Nanoprecipitates to Enhance Radiation Tolerance in High Entropy Alloys

Boopathy Kombaiah^{1,2,*}, Yufan Zhou¹, Ke Jin¹, Anus Manzoor³, Jonathan D Poplawsky⁴, Jeffery A Aguiar⁶, Hongbin Bei⁷, Dilpuneet S. Aidhy⁸, Philip D Edmondson^{1,5}, Yanwen Zhang^{1,9,#}

¹Materials Science and Technology Division, Oak Ridge National Laboratory, Oak Ridge, TN 37831, USA

²Characterization and Post-Irradiation Examination Division, Idaho National Laboratory, Idaho Falls, ID 83415, USA

³Department of Mechanical Engineering, University of Wyoming, Laramie, WY 82071, USA

⁴Center for Nanophase Materials Sciences, Oak Ridge National Laboratory, Oak Ridge, TN 37831, USA

⁵Photon Science Institute, The University of Manchester, Department of Materials, Oxford Road, Manchester, M13 9PL, UK

⁶Nuclear Science and Technology Division, Idaho National Laboratory, Idaho Falls, ID 83415, USA

⁷ School of Materials Science and Engineering, Zhejiang University, Hangzhou 310027, China

⁸Department of Materials Science and Engineering, Clemson University, Clemson, SC 29634.

⁹Department of Materials Science and Engineering, University of Tennessee, Knoxville, TN 37996, USA

#Current address: Condensed Matter Physics, Energy and Environment Science & Technology, Idaho National Laboratory, Idaho Falls, ID 83415, USA

***Corresponding author. Email: boopathy.kombaiah@inl.gov**

Keywords: High entropy alloys, nanoprecipitates, radiation, swelling, hardening, transmission electron microscopy, atom probe tomography, density functional theory

ABSTRACT

The growth of advanced energy technologies for power generation is enabled by the design, development, and integration of structural materials that can withstand extreme environments, such as high temperatures, radiation damage, and corrosion. High entropy alloys (HEAs) are a class of structural materials in which suitable chemical elements in four or more numbers are mixed to typically produce single-phase concentrated solid solution alloys (CSAs). Many of these alloys exhibit good radiation tolerance like limited void swelling and hardening up to relatively medium radiation doses (tens of displacements per atom (dpa)); however, at higher radiation damage levels (> 50 dpa), some HEAs suffer from considerable void swelling limiting their near-term acceptance for advanced nuclear reactor concepts. In this study, we developed a HEA containing a high density of Cu-rich nanoprecipitates distributed in the HEA matrix. The Cu-added HEA, NiCoFeCrCu_{0.12}, shows excellent void swelling resistance and negligible radiation-induced hardening upon irradiation up to high radiation doses (i.e., higher than 100 dpa). The void swelling resistance of the alloy is measured to be significantly better than NiCoFeCr CSA and austenitic stainless steels. Density functional theory simulations predict lower vacancy and interstitial formation energies at the coherent interfaces between Cu-rich nanoprecipitates and the HEA matrix. The alloy maintained a high sink strength achieved via nanoprecipitates and the coherent interface with the matrix at a high radiation dose (~50 dpa). From our experiments and simulations, the effective recombination of radiation-produced vacancies and interstitials at the coherent

interfaces of the nanoprecipitates is suggested to be the critical mechanism responsible for the radiation tolerance of the alloy. The materials design strategy based on incorporating a high density of interfaces can be applied to high entropy alloy systems to improve their radiation tolerance.

INTRODUCTION

Nuclear energy has become an essential option for producing carbon-free energy with the potential capacity to ensure global energy security^{1,2}. Successful design and deployment of advanced nuclear reactor concepts are critical to generating nuclear power and propulsion that is sustainable, economical, safe, and proliferation-resistant . In contrast to present-generation terrestrial light-water reactors (LWR), advanced reactor and propulsion concepts are required to operate at much higher temperatures (up to 1000 °C), and higher irradiation doses (up to 200 displacements per atom, dpa), and under extreme environments². Such a combination of radiation damage and thermal exposure would alter the physical and chemical characteristics of structural materials, leading to void swelling, radiation hardening, and radiation-induced segregation that affect their structural integrity²⁻⁴. Thus, developing advanced structural materials that can satisfactorily perform for the reactor lifetime under these extreme conditions is critical for successfully deploying advanced reactor and propulsion concepts.

Conventionally, several materials design strategies have been commonly used to enhance the irradiation performance of structural materials. One is choosing appropriate matrix phases in materials to achieve target performance under reactor operation conditions ^{5, 6}. For example, materials with a body-centered cubic (BCC) crystal structure have been demonstrated to exhibit better swelling and hardening resistance under irradiation than those with a face-centered cubic structure (FCC) ⁷. Another common strategy has been designing materials with high sink strength for absorbing defects generated during irradiation. Nanostructured materials such as oxide dispersion strengthened (ODS) steels, alloys with fine precipitates such as Ti modified stainless steel, nanolayered composites, and nanograined materials have demonstrated excellent radiation-resistant properties compared to conventional materials ^{5, 6, 8-12}. In these materials, the presence of a high density of point-defect sinks in the form of grain boundaries and phase interfaces has been ascribed to the increased radiation tolerance ¹³. However, these materials may pose some processing and manufacturing challenges through conventional methods for making engineering scale components ^{14, 15}.

Recent demonstrations of notable radiation-tolerant properties of high entropy alloys (HEAs) or multi-principal elements alloys (MPEAs) showcase a materials design strategy in which more suitable alloying elements (>4) are mixed to produce single-phase concentrated solid solution alloys (SP-CSAs) ¹⁶⁻²¹. In addition to radiation tolerance, HEAs have desirable properties such as good mechanical

strength, ductility, and corrosion resistance with potential applications as structural alloys in extreme environments^{19, 22}. For instance, the FeNiMnCr HEA showed improved radiation tolerance, such as reduced void swelling, radiation-induced segregation, and hardening compared to conventional Fe-Cr-Ni alloys within a 400-700 °C temperature range and at 10 dpa¹⁷. Similarly, under irradiations up to 53 dpa at elevated temperatures, NiCoFeCr HEA exhibited ~3 and 10 times lower swelling than equiatomic NiCoCr and NiCo SP-CSAs, respectively^{23, 24}.

In contrast to the conventional alloys that usually contain two or three significant elements, HEAs contain multiple principal elements in equiatomic or near equiatomic composition and have enabled an enormous opportunity for tailoring intrinsic materials properties²⁵. In other words, SP-CSAs allow scientific efforts at the most fundamental level, as the influence of chemical disorder can be emphasized or deemphasized through appropriate choices of alloying elements in FCC and BCC CSAs²⁵. A systematic increase in the number of suitable elements, more accurately increasing the level of chemical disorder from pure metals, has been shown using computational modeling and experiments to decrease the transport properties such as thermal and electrical conductivity¹⁹. The level of chemical disorder depends substantively on specific alloying elements rather than the number of alloying elements²⁵. The decreasing trend in the transport properties is ascribed to the enhanced electronic and phonon scattering phenomena due to the increased chemical disordering and lattice distortion as more selective alloying

elements are added to the material system. Consequently, ion-atom interaction during irradiation has been argued to produce pronounced local thermal spikes in concentrated alloys due to more confined energy dissipation leading to enhanced defect recombination and decreased damage accumulation¹⁹. Furthermore, experiments and computational modeling have demonstrated reduced defect mobility and altered migration paths that favor efficient vacancy-interstitial recombination in concentrated alloys during irradiation. Thus, HEAs exhibit improved radiation tolerance with resistance to void swelling and radiation-induced hardening and segregation^{16, 23}.

However, the radiation-tolerance properties of some HEAs have been found to diminish as radiation damage accumulates (>50 dpa) with a marked void swelling under irradiation and potentially secondary phase formation^{23, 26, 27}. As a result, relying on tailoring alloy composition as the sole design strategy for HEAs operating under high radiation doses, i.e., advanced nuclear reactor concepts (> 200 dpa), becomes unviable². In this study, we demonstrate a materials design strategy in which we synergistically combine the benefit of alloy complexity, i.e., HEAs, with incorporating a high density of interfaces in the microstructure for producing a HEA with extraordinary radiation tolerance up to 500 dpa. El-Atwani et al. demonstrated near negligible irradiation hardening in tungsten-based BCC alloys at 1073 K up to 8 dpa and rationalized the behavior to the formation of Cr- and V-rich second phase particles that could facilitate point defects recombination²¹. In FCC HEAs, Chen et

al. performed helium ion irradiation on NiCoFeCr HEA with 5 at. % of minor elements such as Cu, Al, and Ti, and found that the alloys with minor elements produced higher bubble swelling than the parent alloy ²⁸. Similar approaches have been applied to HEAs through precipitation-hardening to improve their room temperature and high-temperature mechanical properties ²⁹⁻³¹. For instance, Liang et al. and Yang et al. demonstrated this materials design strategy by incorporating nanoprecipitates with coherent interfaces in complex alloys such as HEAs to achieve ultrahigh strength without trading off ductility ^{32, 33}. The nanoprecipitates or second phases in these alloys systems have been shown to interact with the deformation processes to increase the work hardening rate, thus imparting ductility in the alloys. In another recent study, Yang et al. incorporated nanoprecipitates to strengthen and add ductility to a medium entropy alloy by controlling the phase transformation characteristics during deformation ³¹. Incorporating interfaces in conventional materials is an efficient design strategy for improved radiation tolerance in the nanostructured materials ^{34, 35}. Nanostructured materials, such as nanograined and nanolayered materials, contain a high density of interfaces acting as defect sinks for absorbing point defects generated during irradiation, which imparts excellent radiation tolerance. In our approach, NiCoFeCr alloy was doped with 3 at.% of Cu (NiCoFeCrCu_{0.12}) using the floating-zone solidification method and subsequentially heat treated to form a multicomponent alloy that has a high number density of Cu-rich nanoprecipitates. We show that the combination of compositional

complexity using suitable multi-principal alloying elements and an increased number density of nanoprecipitates that act as defect sinks enhance the radiation tolerance of NiCoFeCrCu_{0.12} even at higher damage levels. We have carried out a systematic experimental and atomistic modeling approach to demonstrate the excellent radiation tolerance of NiCoFeCrCu_{0.12} HEA. The experimental work involved the design and synthesis of the alloy, irradiation under various conditions, and pre-irradiation and post-irradiation examination of the alloy using advanced characterization techniques like transmission electron microscopy (TEM) and atom-probe tomography (APT). We complemented our experimental results with density functional theory (DFT) simulation methods to uncover the point defect behavior at the interfaces of Cu-rich nanoprecipitates and the HEA matrix that can be linked to the radiation performance of the alloy.

MATERIALS AND METHODS

Material Synthesis. Equiautomic NiCoFeCr and NiCoFeCr-3 at.% Cu (NiCoFeCrCu_{0.12}) were produced through the casting and direction solidification route in this study. Elements (Ni, Co, Fe, Cr, and Cu) with more than 99.9% purity were mixed to attain the required composition and melted using the arc melting process. Once solidified, the alloy piece was flipped and melted again. This process was repeated five more times to ensure the complete mixing of the elements in the alloy. The NiCoFeCr alloy was directly cast into an ingot form, whereas single crystal

rods of Cu-added multicomponent alloy were grown using the floating-zone directional solidification method.

Irradiation Procedure. For preparing the specimens for irradiation, the alloys were metallographically polished using colloidal silica to a surface roughness below 3 nm. The samples of size about 5 mm × 5 mm × 1 mm were irradiated with 3 MeV Ni²⁺ at 500 °C to a fluence of 1×10^{17} /cm² at a beam flux of approximately 2.8×10^{12} ions/cm²/s, accounting for about 10 hrs of irradiation time. Both NiCoFeCr and NiCoFeCr-3 at.% Cu (NiCoFeCrCu_{0.12}) specimens in as-processed conditions were irradiated in one batch to avoid variations in irradiation conditions such as temperature, ion fluence or dose rate.. The Ni beam was defocused to have a broad profile and wobbled over the irradiated area to ensure uniform irradiation with scanning frequencies of 517 and 64 Hz along the horizontal and vertical directions, respectively ³⁶. These irradiation conditions achieved a peak dose of ~106 dpa in the specimens. To achieve high damages in the NiCoFeCrCu_{0.12}, irradiations using heavy ions of 10 MeV Au³⁺ for peak doses of 100 dpa, 350 dpa, and 500 dpa at 475 °C were conducted. Furthermore, we irradiated NiCoFeCr and NiCoFeCrCu_{0.12} alloys with 3 MeV Ni²⁺ at 580 °C to a fluence of 5×10^{16} ions/cm² achieving a peak radiation dose of ~50 dpa. At the end of irradiation, the specimens were cooled down by passing liquid nitrogen through the sample holder closer to room temperature, which would mitigate any thermal-assisted modification of the irradiation microstructure.

The irradiation-induced damage profile and Ni concentration were predicted using the Stopping and Range of Ions in Matter (SRIM) program by choosing the calculation type ‘Ion distribution and quick calculation of damage’³⁷. The target composition was set to be Ni, Co, Fe, and Cr – 24.25 atomic % each – and the remaining Cu and the density of the target was assumed to be 8.8 g/cm³. A value of 40 eV was set for the displacement threshold energy¹⁹. A total count of 10⁵ ions was included in the SRIM calculations. The damage profile, dpa, was determined from the total number of vacancies (produced by Fe, Co, Ni, and Cr recoils) and the replacement collisions. The software directly provided the Ni concentration profile. We applied similar SRIM calculations to the irradiations by Au ions.

Materials Characterization. We prepared the TEM thin foils by applying the Focused Ion Beam (FIB) technique using an FEI Quanta 3D 200i dual-beam Scanning Electron Microscope (SEM) and FIB system available at Low Activation Materials Development and Analysis (LAMDA) Laboratory at the Oak Ridge National Laboratory (ORNL) and Idaho National Laboratory (INL). Subsequently, to minimize the surface damage induced by the FIB sectioning, we polished the thin foil with low energy (900 eV and 600 eV) Ar ions using a model 1040 Fishione nanomill. For imaging, we used a JEOL JEM 2010F TEM. We performed STEM-Energy Dispersive Spectroscopy (EDS) – compositional mapping using an FEI Talos F200X Scanning Transmission Electron Microscope (STEM),

equipped with a Super-X energy dispersive spectrometer system, offering high-quality compositional mapping with a high elemental detection limit. The collected compositional data was in the form of EDS-X-Ray count maps, from which Quantity maps (Q-maps) were calculated using the Espirit-Bruker software by applying the Cliff-Lorimer method for further analysis³⁸. Furthermore, a 200 KeV ThermoFisher probe-corrected Titan TEM at INL was employed for atomic resolution imaging of the precipitate-matrix interface in the NiCoFeCrCu_{0.12} alloy.

We used an FEI Nova 200 dual-beam SEM/FIB to lift out regions of interest, mount sections of the lift out on Si microtips, and fabricate needle-shaped APT specimens using an annular milling pattern and a final 2 kV cleaning step³⁹. We conducted the APT experiment using a CAMECA local electrode atom probe (LEAP) 4000X HR equipped with a reflectron lens. The samples were run at 30K base temperature in laser mode with a 60 pJ laser power, 0.5% detection rate, and a pulse repetition rate, allowing all ions in the mass spectrum to be collected. Finally, we analyzed the data using CAMECA's Integrated Visualization and Analysis Software (IVAS 3.8).

A Nanoindenter XP was utilized for the nanoindentation tests using a Berkovich triangular pyramid indenter to determine the radiation-induced hardening in the alloys. Tests were conducted at a constant $\dot{P}/P = 0.05 \text{ s}^{-1}$ (P is the load). A maximum load of 5 mN corresponding to an indentation depth of ~200-250 nm was applied for hardness measurements. Several indentations were performed on each sample to

allow statistical analysis, and some indents were placed in the pristine region while others were in the irradiated region. Load-displacement data were recorded during nanohardness tests. The hardness data were calculated from the unloading curves based on the classical Oliver-Pharr method ⁴⁰.

Density Functional Theory. Using density functional theory (DFT) calculations, we studied vacancy stability at three interface structures differentiated by alloy chemistry. The interfaces are NiFe | Cu, NiFeCoCr | Cu, and NiFeCoCr | Ni_{0.37}Cu_{0.63}. Each structure consists of 8×2×2 FCC supercell containing 128 atoms. Each of the two materials forms half the supercell, i.e., 4×2×2 containing 64 atoms. Figure 1 shows a schematic representation of the NiFeCoCr | Ni_{0.37}Cu_{0.63} supercell. The Ni_{0.37}Cu_{0.63} system closely represents the major elements in the precipitate chemistry (ratio of Cu to Ni is 1.7) after irradiation up to 106 dpa in the NiCoFeCrCu_{0.12} HEA, which is discussed in section 3.3. The chemical disorder in the structure is introduced using the special quasi-random structure (SQS) method ⁴¹. The SQS algorithm aims to minimize the correlation functions of the first two nearest-neighbor shells. The SQS structures provide a good approximation to near randomness in solid solution alloys.

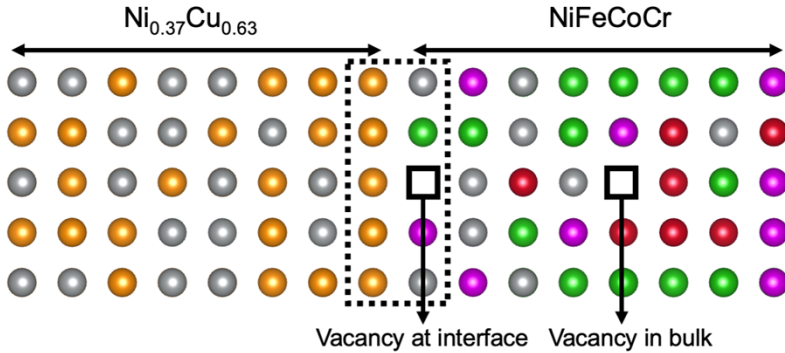


Figure 1. Schematic representation of $\text{NiFeCoCr} \mid \text{Ni}_{0.37}\text{Cu}_{0.63}$ interface. Filled circles are the atomic species, and empty squares are the vacancies. The interface is between $\text{Ni}_{0.37}\text{Cu}_{0.63}$ precipitates (left side) and the NiFeCoCr matrix (right side).

The calculations are performed using Vienna *ab-initio* Software Package (VASP)⁴². The Projector Augmented Wave (PAW) method is employed with Generalized Gradient Approximation- Perdew-Burke-Ernzerhof (GGA-PBE) exchange-correlation functionals⁴². The Brillouin zone is sampled with a $2 \times 4 \times 4$ Monkhorst-Pack (MP) mesh, and the energy cut-off of the wave functions is taken as 500 eV for all calculations⁴³. The Methfessel-Paxton technique with a smearing width of 0.1 eV is used, and the structures are relaxed until the criteria for forces is smaller than 0.03 eV/ \AA ⁴⁴.

The stability of a vacancy at the interface or in bulk is calculated by comparing the total energies of the two structures, i.e., by placing a vacancy at the interface compared to inside the bulk. The vacancy stability is calculated for all four elements in the alloy, i.e., Ni, Fe, Cr, and Co. To capture the statistical variations due to the

chemical disorder in the alloy, we have performed calculations on two different SQS structures for each interface structure. In addition, we have created three different vacancies of each element in a given SQS structure, both in bulk and at the interface. The vacancy stability (ΔE) is given by equation (1).

$$\Delta E = E_{\text{bulk}} - E_{\text{interface}} \quad (1)$$

where E_{bulk} and $E_{\text{interface}}$ are the total structure energies when a vacancy is placed in the bulk and interface, respectively. Similarly, we carried out calculations to understand the interstitial stability at the Ni | Cu interface. Different interstitials are tested i.e., octahedral, and dumbbells, i.e., [100], [001], [110], [001] and [111]. The difference between [001] and [100] is that both interstitial atoms are ^{the} first nearest neighbors to Cu atoms in [001] dumbbell, whereas they are not in [100] dumbbell, as shown in Figure 2.

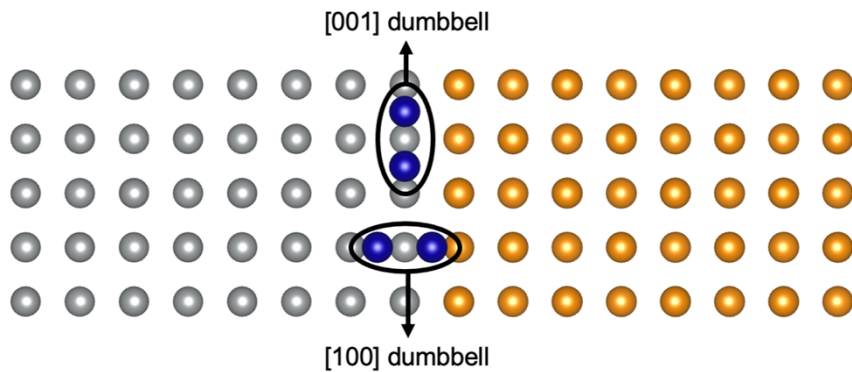


Figure 2. Schematic representation of $[100]^{\text{Ni-Ni}}$ and $[001]^{\text{Ni-Ni}}$ interstitials in Ni | Cu interface. Gray and yellow atoms are the Ni and Cu atoms at lattice sites whereas blue atoms are the Ni-Ni interstitials.

RESULTS

Pre-Irradiation Microstructure. In the as-grown state, the Cu-added HEA formed an FCC single crystal as exhibited by the X-Ray Laue backscattering pattern along the [100] direction (Figure 3). Bulk scale to nanoscale characterization techniques, such as 2D-synchotron X-ray diffraction (XRD), SEM backscattered images, energy dispersive X-Ray spectroscopy (EDS) maps, and scanning transmission electron microscope (STEM) – EDS maps, revealed a single phase NiCoFeCrCu_{0.12} alloy, indicating that Cu completely dissolved in the solid solution (Figures 3). However, after annealing at 500 °C for 10 hrs, Cu-rich nanoprecipitates formed in the NiCoFeCrCu_{0.12} HEA distributed uniformly in the matrix with a high number density (Figure 4). From TEM selected area diffraction (SAD) and XRD data of the annealed NiCoFeCrCu_{0.12}, the Cu-rich precipitates exhibit no extra diffraction points indicating a similar lattice parameter between the matrix and the precipitates (3.5878 Å) (Figure S1). It also indicates that the interface between the Cu-rich nanoprecipitates and the matrix is coherent with atomic positions of both phases matching. The chemical composition, as well as the physical characteristics of the precipitates, were calculated from the reconstruction of the APT data ⁴⁵. The number density and the average (mean) diameter of the precipitates obtained from the APT data are $1.3 \times 10^{24} /m^3$ and 3 nm, respectively ⁴⁶. The volume fraction of the Cu nanoprecipitates was estimated to be 4.9%. The bulk composition of the NiCoFeCrCu_{0.12} is estimated to be Ni-23.3, Co-25.3, Fe-24.7, Cr-24.0 and Cu-2.7 (at.

%). The average composition of around 10 precipitates extracted from the APT data is Ni-20.1, Co-20.1, Fe-20.7, Cr-17.6, and Cu-21.5 (at.%). On the other hand, the equiatomic NiCoFeCr HEA is FCC solid solution with no precipitates or nanoclusters⁴⁷.

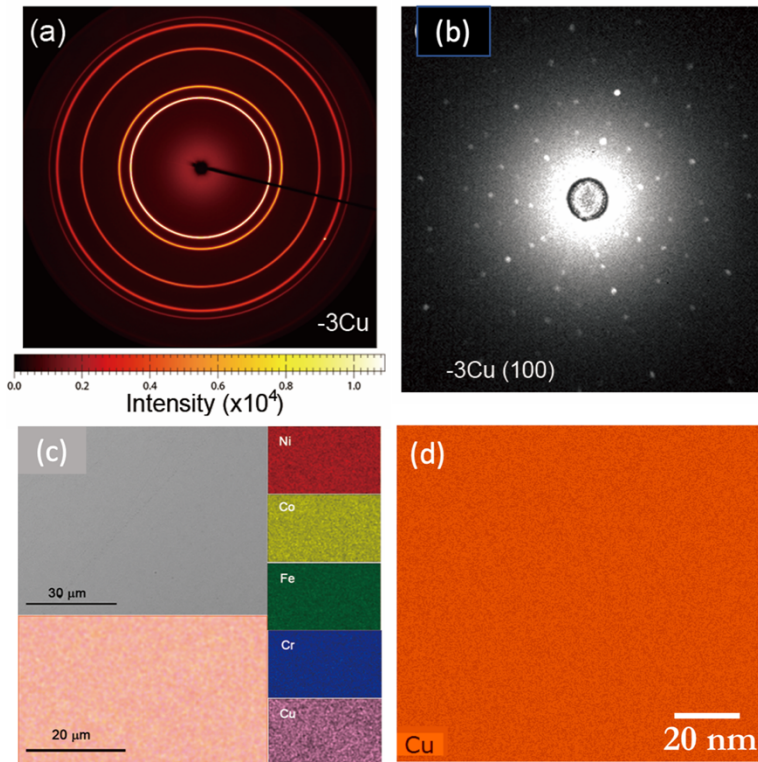


Figure 3: (a-d) Microstructure of the as-prepared $\text{NiCoFeCrCu}_{0.12}$ multicomponent alloy: (a) Synchrotron X-Ray diffraction pattern, (b) X-Ray Laue backscattering pattern, (c) Scanning Electron Microscopy (SEM)-EDS maps, (d) STEM-EDS Cu elemental map shows Cu uniformly distributed in the solid solution in the as-cast alloy.

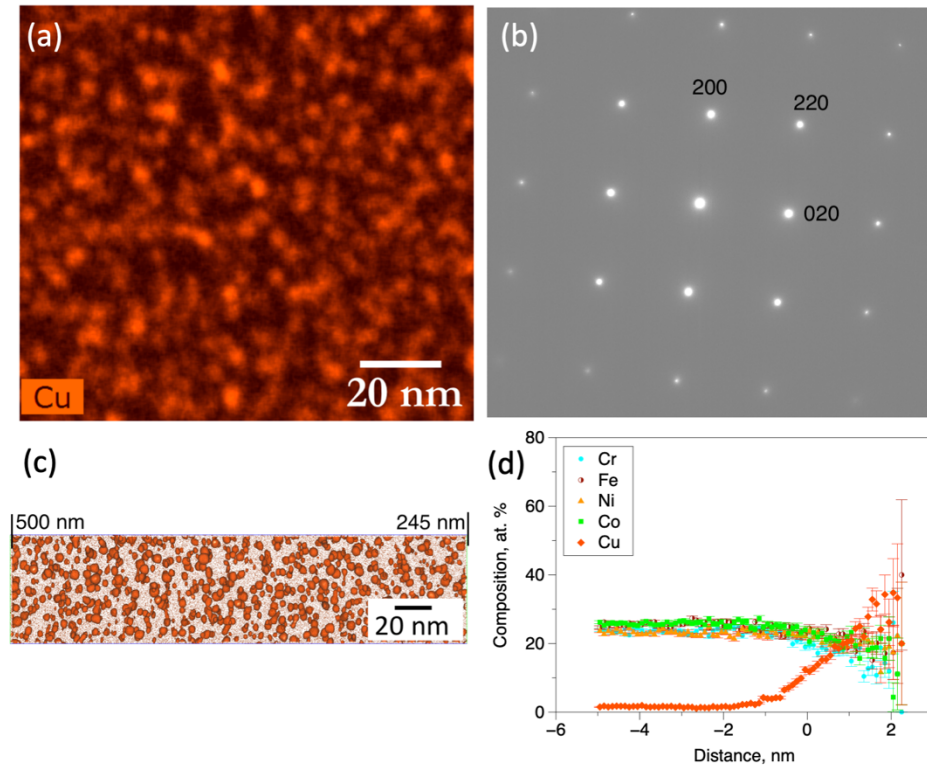


Figure 4. (a) NiCoFeCrCu_{0.12} alloy annealed at 500 ° C for 10 hrs resulted in the formation of a high density of Cu-rich nanoprecipitates, (b) Selected area diffraction pattern along <001> zone-axis diffraction reveals no extra diffraction points indicating similar lattice parameters between the matrix and the precipitates. (c) 10 at.% isosurface concentration diagram extracted from the Atom-probe tomography data shows the presence of Cu-rich nanoprecipitates in the depth range of 245 nm-500 nm. (d) APT data reconstruction shows the average composition profile through 10 precipitates.

Irradiation Performance of NiCoFeCrCu_{0.12}. NiCoFeCrCu_{0.12} outperformed the equiatomic NiCoFeCr HEA under the ion-irradiation conditions employed in our investigation with superior void swelling resistance and low radiation hardening. For

instance, after 3 MeV Ni²⁺ irradiation up to a peak dose of 106 dpa at 500 °C, NiCoFeCrCu_{0.12} HEA developed no voids up to the peak dose region and only a few small voids in the region beyond the peak dose, as revealed by the TEM bright field images. The void images were recorded by tilting the specimen from diffracting conditions to minimize the contrast of dislocations arising due to diffraction contrast (Figure 5). However, a higher number density of larger voids was present in the irradiated region of NiCoFeCr alloy resulting in significant volumetric swelling (Figure 5). Furthermore, we calculated the percentage of void swelling in the irradiated alloys by measuring the void size, the number of voids, and the thickness of TEM specimens using energy-filtered transmission electron microscopy (EFTEM) mapping. By assuming that the voids are spherical in shape, we calculated the volume of each void (V_i). Further, we calculated the percentage of void swelling (s) by using Eqn (1),

$$s = \frac{\sum_{i=1}^n V_i}{V_t - \sum_{i=1}^n V_i} \times 100$$

where, V_t is the TEM specimen volume in which the voids are distributed. By this method, the percentage of void swelling in the NiCoFeCrCu_{0.12} (0.02%) is approximately two orders of magnitude lesser than that in NiCoFeCr (3.1%) (Figure 6).

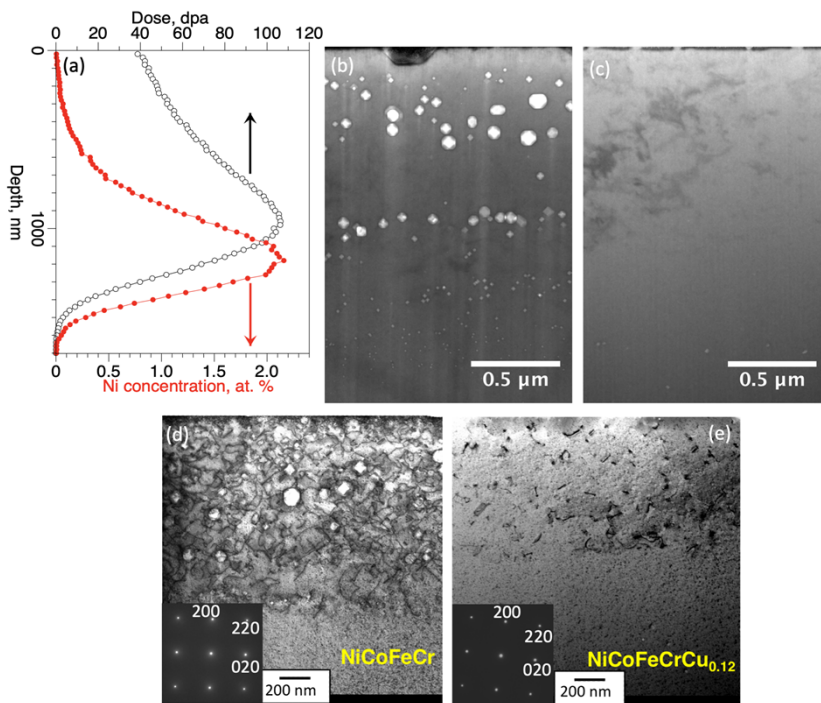


Figure 5: (a) Distribution of damage in terms of dose and injected Ni ion concentration as a function of depth calculated using SRIM for 3 MeV Ni^{2+} irradiation at 500 °C to a fluence of 1×10^{17} ions/cm². The peak dose of 106 dpa occurs at around 1000 nm, and the implanted Ni ion concentration peaks at 2.2 at. % at 1200 nm depth. (b-c) TEM-bright field images of NiCoFeCr and NiCoFeCrCu_{0.12} taken under a non-diffracting condition showing the distribution of voids in the samples, (d-e) STEM-Bright field images recorded under the [001] zone-axis condition showing dislocations produced by the irradiation.

Similarly, we quantified the radiation-induced dislocation density in both alloys by measuring the total dislocation length in the irradiated region by tracing dislocation lines using ImageJ software. The thicknesses of the irradiated region in TEM foils

were measured using the Energy Filtered Transmission Electron Microscopy (EFTEM) method. The dislocation density was calculated by dividing the total dislocation line length by the volume of the TEM foil. For a proper comparison of the dislocation density, the TEM specimens were tilted to <001> zone axis to include most dislocations in the STEM-bright images (Figure 5). We could make two observations from this analysis: 1) the dislocation density in the irradiated NiCoFeCr ($1.5 \times 10^{14} /m^2$) was about two orders of magnitude higher than that present in the NiCoFeCrCu_{0.12} ($6 \times 10^{12} /m^2$); 2) dislocations in NiCoFeCr are composed of large dislocation networks, whereas dislocations in the Cu-added HEA were small loops without much growth. The comparison of void swelling and dislocation density between NiCoFeCr and NiCoFeCrCu_{0.12} and the hardness changes in the alloys as a function of dose are provided in Figure 6. While the hardness of NiCoFeCr increased with radiation damage, the NiCoFeCrCu_{0.12} remains constant, indicating negligible radiation-induced hardening in the Cu-added HEA. It should be noted that the radiation-induced hardening in NiCoFeCr could be produced by the high dislocation density, and voids⁴⁸. Furthermore, radiation-produced smaller defects such as point defects (vacancies and interstitials) and their clusters invisible to TEM-based techniques can also contribute to materials' hardness⁴⁹. The effect of voids on hardness in irradiated materials is not straightforward. Small voids usually act as obstacles to dislocation movement, causing strengthening of materials⁵⁰; on the other hand, very large voids (mimicking

porous materials) can degrade the hardness by reducing the elastic modulus of materials^{51, 52}. However, a detailed analysis of void-induced hardening or softening in NiCoFeCr HEA is beyond the scope of this study.

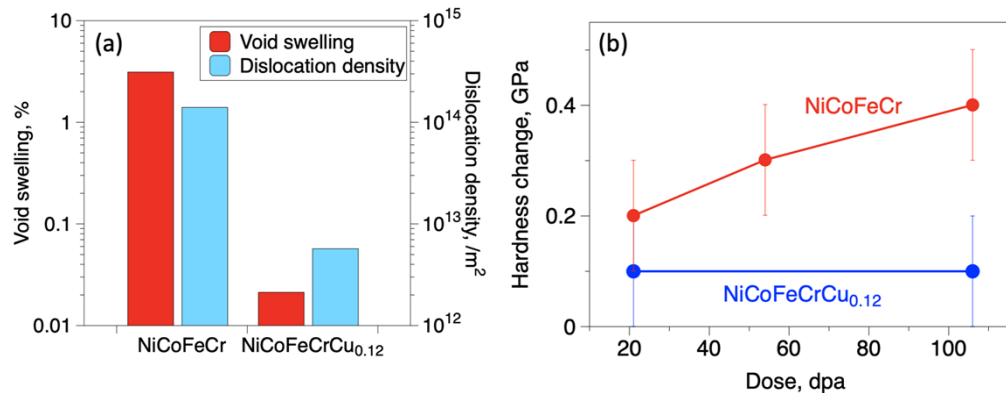


Figure 6: (a) Void swelling and dislocation density resulted from the irradiation at 500 °C and ~106 dpa compared between NiCoFeCr and NiCoFeCrCu_{0.12} HEAs, (b) Hardness change in the HEAs as a function of irradiation dose at 500 °C.

Post-irradiation examination of NiCoFeCr and NiCoFeCrCu_{0.12} at 580 °C and a maximum dose of 50 dpa also reveals that the latter alloy exhibited negligible swelling. In contrast, the former alloy swelled 1.2% through void formation under the irradiation condition (Figure S2)²³. Similarly, in the NiCoFeCrCu_{0.12} samples irradiated to higher doses (100 dpa, 350 dpa, and 500 dpa) with Au ions at 475 °C, no considerable void swelling (<0.01 %) was noted, portraying the remarkable void swelling resistance of the alloy (Figure S3). We compared the void swelling in the HEAs with other structural alloys such as austenitic stainless steel, ferritic steel⁵³, and oxide-dispersion strengthened (ODS) steels ion-irradiated to different doses

close to their peak void swelling temperatures (Figure 7). We can observe from the plot that the NiCoFeCrCu_{0.12} seems to exhibit outstanding void-swelling resistance, better than that of the FCC single-phase high entropy alloys, body-centered cubic steels, austenitic steels, and ODS-steels that are known for their swelling resistance under irradiation. We emphasize that the NiCoFeCrCu_{0.12} has an FCC crystal structure typically known for its lack of swelling resistance ². A classic example would be austenitic stainless steel which significantly swells under irradiation conditions ⁷.

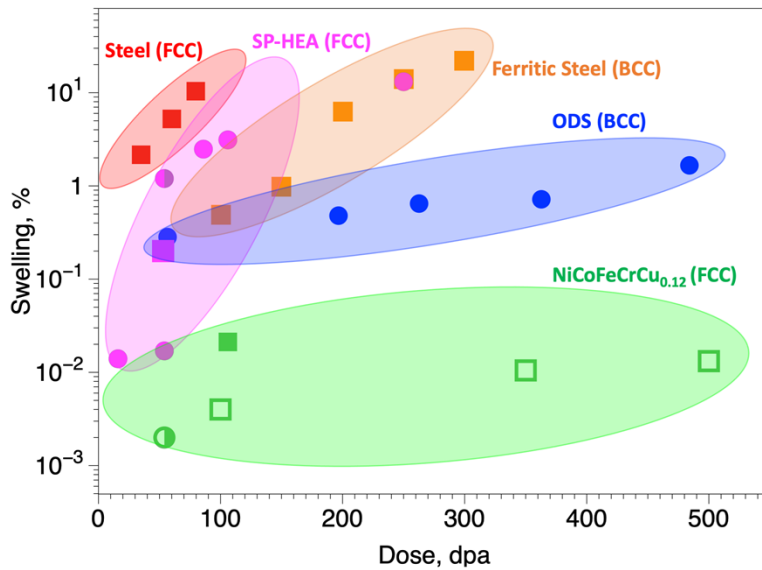


Figure 7: Void swelling of various ion-irradiated structural alloys is compared with NiCoFeCrCu_{0.12} HEA as a function of radiation dose. The irradiation temperatures are in the range of 475 – 500 °C. 12Cr-ODS alloy (475 °C) ⁵⁴, EP-450 Ferritic steel (480 °C) ⁵³, 304L stainless steel (500 °C) ⁸, single-phase HEA (SP-HEA) such as NiCoFeCrMn (500 °C) ¹⁶ and NiCoFeCr (500 °C and 580 °C)-This study, and NiCoFeCrCu_{0.12} (475 °C, 500 °C, and 580 °C)-This study.

Nanoprecipitates Stability upon Irradiation. The APT data obtained from the irradiated NiCoFeCrCu_{0.12} samples show how the physical and chemical characteristics of the Cu-rich precipitates change from irradiation. From the STEM-EDS maps obtained from the non-irradiated and irradiated NiCoFeCrCu_{0.12} (Figures 4 & 8), we observed the average size of the Cu-rich nanoprecipitates became larger, and the number density of the precipitates got reduced after irradiation. From the APT data analysis, we obtained the average diameter, number density, and volume fraction of the Cu-rich nanoprecipitates to be 5.4 nm, $2.1 \times 10^{23} /m^3$, and 1.9, respectively. As seen in Table 1, the APT data analysis revealed a similar trend of precipitate growth and reduced number density by an order of magnitude due to irradiation. We can note that the ion irradiation decreased the volume fraction of the precipitates compared to the non-irradiated NiCoFeCrCu_{0.12} by almost half. Similarly, Cu-rich nanoprecipitates remained chemically stable after Au ion irradiation up to a dose of 500 dpa at 475 °C (Figure S4). However, a fraction of nanoprecipitates started showing physical changes like elongation at 500 dpa (Figure S4). In addition to the change in the physical characteristics of the precipitates, according to the APT data, irradiation modified the chemical composition of the precipitates (Figure 8 & Table 1). The precipitates in the irradiated alloy are enriched with Cu (~50 at.%) and Ni (~30 at.%), while the remaining elements contribute to about 6-7 at.% each. Notably, no new radiation-induced phases were observed in the irradiated

NiCoFeCrCu_{0.12} under the irradiation conditions explored in this study. On the other hand, as per the APT data, the single phase in the NiCoFeCr alloy remained chemically stable under irradiation except for segregation around the voids observed from the STEM-EDS maps (Figure S5). Here, we underscore the observations of Fan et al. that the transition from suppressed void growth to significant void swelling in HEAs is attributed to dislocation evolution and local chemical inhomogeneity (enrichment of Fe/Cr in the matrix) at higher doses²³. The excellent void swelling resistance of NiCoFeCrCu_{0.12} at higher doses agrees with the observation of Fan et al. as the efficient recombination of vacancies and interstitials mitigates any notable dislocation evolution and void development and the associated radiation-induced segregation around the voids.

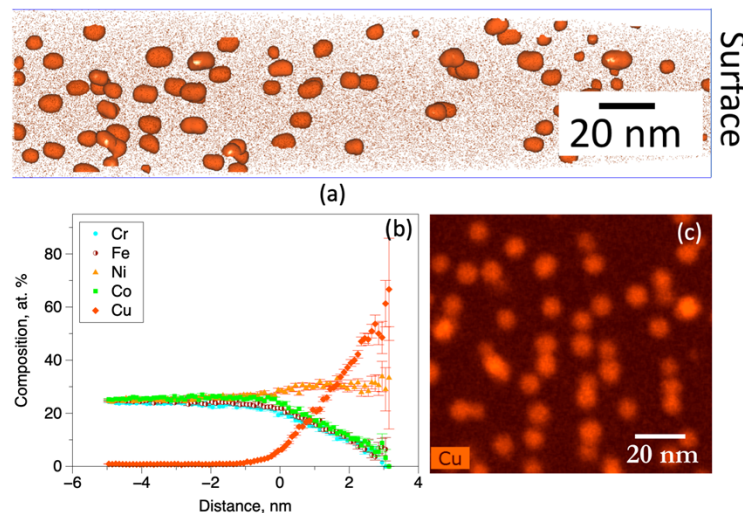


Figure 8: (a) 10 at.% isosurface concentration diagram extracted from the Atom-probe tomography data of the irradiated NiCoFeCrCu_{0.12} alloy in the irradiation depth range of 70-260 nm. (b) APT data reconstruction shows the average composition

profile through 10 precipitates. (c) STEM-EDS map showing Cu elemental distribution reveals the presence of the Cu-enriched precipitates.

Table 1: Physical characteristics of the Cu-rich second phase calculated from the APT data

	Average Diameter, nm	Number Density, m ³	Volume fraction
NiCoFeCrCu _{0.12} – Annealed at 500 ° C for 10 hrs	3	1.30 × 10 ²⁴	4.9
NiCoFeCrCu _{0.12} – Irradiated (500 ° C and 106 dpa)	5.4	2.10 × 10 ²³	1.9

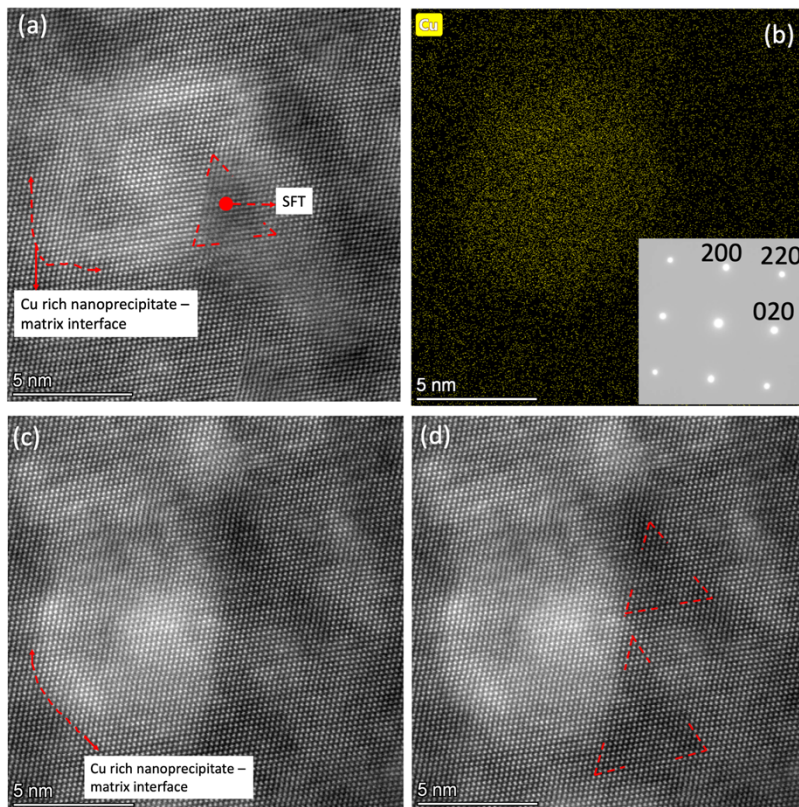


Figure 9: STEM-HAADF atomic resolution images showing a Cu-rich precipitate in the matrix of irradiated NiCoFeCrCu_{0.12} HEA (580 °C and 54 dpa). (a) The Cu-rich precipitate has brighter contrast, and its interface with the matrix is partly marked using a red-dashed line. We can see that the precipitate-matrix interface maintains coherency post-irradiation. Also, a stacking fault tetrahedron (SFT) situated close to the interface is marked. (b) STEM-EDS map recorded at the same location as (a) showing Cu-rich region. The inset shows the selected area diffraction pattern recorded from the irradiated region of NiCoFeCrCu_{0.12} HEA. (c) The interface of another Cu-rich precipitate with brighter contrast is marked using a red-dashed line. (d) Two vacancy-based SFT located close to the Cu-rich precipitate pointed out in (c) are marked in red-dashed lines.

Stability of the Precipitate-Matrix Interfacial Coherency. The stability of lattice coherency of interfaces in materials under irradiation is an important factor shaping their radiation tolerance since the characteristics of interfaces influence the absorption and recombination behavior of point defects ^{9, 55}. For instance, Vattre et al. demonstrated using object kinetic Monte Carlo simulations that the sink strength of interfaces varies as a function of the interfacial elastic field that mainly depends on the interface coherency ⁵⁵. In our study, STEM-HAADF atomic resolution imaging was used to characterize the nanoprecipitate-matrix interfaces in the 3 MeV Ni²⁺ irradiated NiCoFeCrCu_{0.12} HEA at 580 °C with a peak dose of 50 dpa (Figure 9). We

can note that the interface maintains atomic coherency in agreement with the observation from the TEM selected area diffraction (Figure 5) and XRD results (Figure S1) that reveal similar lattice parameters of the matrix and the nanoprecipitates. Notably, our observation stands different from earlier studies on irradiation effects on the precipitate-matrix coherency in other material systems, which have shown loss of coherency upon low dose irradiation (<0.01 dpa) in copper alloys containing coherent precipitates^{56, 57}. For example, Wang et al. noted the loss of precipitate coherency in the Cu-Co system induced by an irradiation dose of ~0.01 dpa for precipitate sink strengths of up to $6 \times 10^{13} /m^2$. In contrast, higher doses (~1 dpa) were necessary for coherency loss in the material with larger sink strength ($>10^{14} /m^2$). The study, with support of computational modeling, has suggested that biased absorption of self-interstitial atoms at the interfaces in low sink strength materials leads to the loss of coherency at lower doses, in line with previous studies⁵⁶⁻⁵⁸. However, the coherency at the precipitate-matrix interface is maintained in NiCoFeCrCu_{0.12} HEA at comparably high doses (~50 dpa), indicating good stability of the interfaces under irradiation in the alloy. The interfacial stability could be ascribed to the efficient recombination of radiation-induced vacancies and interstitials at the interface. Plus, a higher sink strength of the nanoprecipitates in NiCoFeCrCu_{0.12} alloy could favor unbiased absorption of both vacancies and interstitials due to the increased probability of vacancies diffusing to the interface⁵⁹. Furthermore, we observed some vacancy-based stacking fault tetrahedra (SFT)

situated close to the nanoprecipitate and matrix interface. Such SFT could have been formed due to the agglomeration of vacancies produced from the irradiation cascades^{60, 61}.

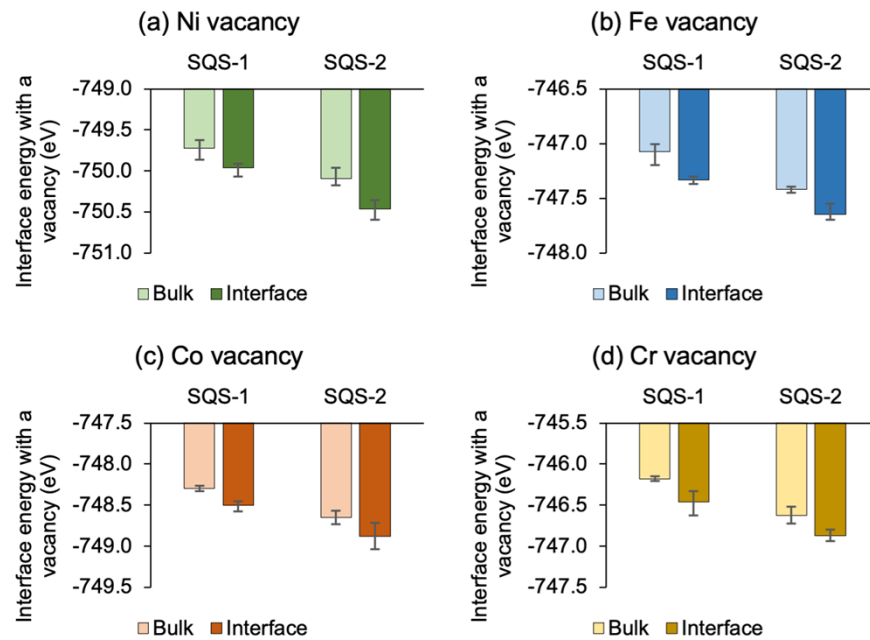


Figure 10: Energy of NiFeCoCr | Ni_{0.37}Cu_{0.63} interface when an atom is removed to create a vacancy, (a) Ni vacancy, (b) Fe vacancy, (c) Co vacancy, and (d) Cr vacancy. The bars show the average energy when vacancy is created at 3 different sites in bulk and at the interface. The error bars show the maximum and minimum energies of the 3 sites considered in the interface. For all the elements, the energy of an interface is low when a vacancy is present at the interface compared to bulk.

Point Defect Stability at Phase Interfaces. We hypothesize that efficient recombination of vacancies and interstitials produced from cascade events is facilitated by the interfaces of Cu-rich nano precipitates and the matrix. To test the hypothesis, we compare the stability of point defects in the bulk and at interfaces to determine the thermodynamic feasibility of absorbing the point defects, which may reveal insights into the swelling resistance of NiCoFeCrCu_{0.12}. Figure 10 compares the system energy of the NiFeCoCr/Ni_{0.37}Cu_{0.63} interface when a vacancy is present at the interface and in the bulk NiCoFeCr matrix, respectively. A coherent precipitate matrix is applied in the SQSs corresponding to the observation made from the atomic-resolution images of the interfaces in the irradiated alloy (Figure 9). One by one, all four elements, i.e., Ni, Fe, Co, and Cr, from the matrix are removed to create a vacancy, and the energy of the interface with the type of a corresponding vacancy is reported in Figures 10 (a) – (d). The bars show the average energy when a vacancy is created at three different sites, each in bulk and at the interface. The error bars show the maximum and minimum energies of the three sites considered at the interface. The energy of the system with the vacancy at the interface is lower than the bulk for all elements, as shown in Figures 10 (a) – (d). Similarly, we have calculated the vacancy stability in other interface systems, i.e., NiFe | Cu and NiFeCoCr | Cu. Table 2 shows ΔE (see equation 1) for all four elements in the two SQS structures in all three interface systems. Here, for each element, the average ΔE is shown, i.e., the average ΔE of the three vacancies in each SQS structure for a

given element. The positive value of ΔE indicates that the vacancy would be more stable at the interface than in bulk. It is observed that the vacancy is stable at the interface for all calculated interfaces for all four elements. In addition, among all interfaces, the vacancy stability is highest for the NiFeCrCo | Cu interface, as shown in Table 2. These results indicate that vacancies are more stable at the interface than in bulk, and the interface acts as a sink to the vacancies.

Table 2: Vacancy stability (ΔE) when a vacancy is present at the interface and in bulk for Ni, Fe, Co, and Cr vacancy in NiFe-Cu, NiFeCoCr-Cu, and NiFeCoCr-NiCu interfaces. The ΔE is expressed in eV.

Interface	Ni vacancy		Fe vacancy		Co vacancy		Cr vacancy	
	SQS-1	SQS-2	SQS-1	SQS-2	SQS-1	SQS-2	SQS-1	SQS-2
NiFe Cu	0.31	0.27	0.34	0.29				
NiFeCoCr Cu	0.41	0.45	0.43	0.43	0.41	0.47	0.55	0.58
NiFeCoCr NiCu	0.25	0.37	0.26	0.23	0.20	0.23	0.28	0.25

It has been shown in previous studies that the formation energy of point defects is lower at interfaces and grain boundaries. Suzuki and Mishin ⁶² calculated the formation energy of vacancies and interstitials at several grain boundaries in Cu and Al and showed low formation energies at grain boundaries compared to the bulk. Using atomistic simulations in Au | Si interface, Navale and Demkowicz ⁶³

showed that the formation energies of both point defects, i.e., vacancies and interstitials, are lower near the interface than in bulk. Similarly, calculations on the Cu | Nb interface by Metsanurk et al. [36] also showed that the formation energy of a Cu vacancy at the interface is lower (0.37 eV at the interface compared to 1.17 eV in bulk). Our results shown in Figure 10 agree with these previous works illustrating that the vacancy formation energies are lower at the interfaces.

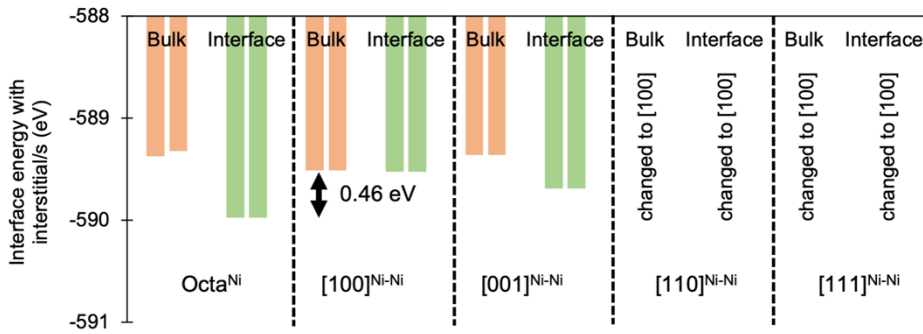


Figure 11: The energy of the Ni | Cu interface when interstitial is in bulk Ni and at the interface. $[100]^{Ni-Ni}$ interstitials are the lowest configuration in bulk. In contrast, the octa^{Ni} is the lowest energy configuration at the interface, which shows octa^{Ni} is the most stable interstitial in this interface and the difference between bulk and interface is 0.46 eV.

Similarly, we have computed the stability of interstitials in a simpler Ni | Cu interface. Figure 11 shows the energy of the Ni | Cu interface when a Ni interstitial is placed inside the bulk and at the interface. Various interstitial configurations, including octahedral and dumbbell, are modeled. We note that $[100]^{Ni-Ni}$ is the

lowest interstitial configuration in bulk, whereas octahedral Ni is the lowest configuration at the interface, as shown in Figure 11. Furthermore, we find that the [110] and [111] dumbbells change to the [100] configuration upon DFT relaxation, as shown in Figure 11. Based on these calculations, the interstitial is stable at the interface by 0.46 eV compared to the bulk, as shown by the lowest system energy of octahedral-Ni among all in Figure 11. In this work, only the Ni- Cu interface is modeled because there are enormously large possibilities of interstitial configurations at various interfaces, and modeling all of them is beyond the scope of this work. Nevertheless, the calculations provide a first-order approximation of higher interstitial stability at the interface than bulk which provides better opportunities for interstitial-vacancy recombination at interfaces.

DISCUSSION

The irradiation performance of NiCoFeCrCu_{0.12} is superior to that of NiCoFeCr HEA and several nuclear structural alloys in terms of resistance to radiation-induced swelling (Figure 7). Also, the NiCoFeCrCu_{0.12} has about one order of magnitude lesser radiation-induced dislocation loops than NiCoFeCr HEA, leading to significantly low radiation-induced hardening (Figure 6). The fundamental mechanism of swelling and hardening of materials under irradiation can be ascribed to the accumulation of radiation-produced point defects – vacancies and interstitials – to form extended defects such as voids and dislocation loops ⁶⁴. These point

defects are produced by radiation cascades resulting from the interaction between high-energy particles (ions, neutrons, and protons) and the host atoms. As such, radiation cascades produce an equal concentration of vacancies and interstitials in materials in the highly dynamic process. While the agglomeration of vacancies under irradiation facilitates nucleation of voids, void growth is carried forward by a biased influx of vacancies to the void nuclei in higher concentrations than interstitials⁶⁵. In this process, the nature of defect sinks, such as dislocations, voids, grain boundaries, and phase interfaces, in their preference to absorb vacancies and interstitials play a significant role in the swelling process. For instance, dislocations tend to absorb interstitials due to the long-range interaction of their stress fields, resulting in a higher flux of vacancies to voids⁶⁵. In effect, recombining vacancies and interstitials produced by irradiation would reduce swelling and hardening in materials.

Based on the little void swelling and low dislocation density produced by irradiation at high doses in NiCoFeCrCu_{0.12}, one could argue that the recombination of vacancies and interstitials has efficiently taken place, prohibiting the influx of point defects for void and dislocation development. On the other hand, significant void growth and dislocation network development in NiCoFeCr could have resulted from the availability of point defects due to their inefficient recombination at high doses. The main difference between the NiCoFeCrCu_{0.12} and NiCoFeCr HEA is associated with their composition resulting in production of Cu nanoprecipitates. We

added Cu to the NiCoFeCr base alloy because Cu will be immiscible with Co, Fe, and Cr forming separate phases due to the positive formation enthalpy of binary compounds with these alloying elements⁶⁶. It has been demonstrated that higher quantities of Cu (20 at.%) produce bulk FCC second phases in equimolar NiCoFeCrCu HEAs⁶⁷. In our study, we limited the amount of Cu added to the NiCoFeCr alloy to 3 at.% to facilitate the formation of the second phase as nanoprecipitates that maintain FCC crystal structure. The presence of a high density of Cu-rich nanoprecipitates in the NiCoFeCrCu_{0.12} creates a large area of coherent interfaces that act as sinks for radiation-produced point defects, which increases vacancy/interstitial recombination. By using the average diameter (D_p) and the number density (N_p) of Cu-rich nanoprecipitates, we estimated their sink strength (S_p) to be $3.7 \times 10^{16} /m^2$ using the following equation⁵⁶.

$$S_p = 2\pi D_p N_p \quad (2)$$

The high sink strength of NiCoFeCrCu_{0.12} is comparable to MA957-ODS and 14YWT-ODS, which exhibit the best swelling resistance among structural alloys⁵. Furthermore, it is evident from atomic resolution STEM imaging (Figure 9), TEM selected area diffraction pattern analysis, and XRD data (Figure S1) that the Cu-rich nanoprecipitates maintain coherency with the matrix upon irradiation up to the 106 dpa employed in this study. It should be noted that the irradiation processes alter the physical and chemical characteristics of the Cu-rich nanoprecipitates. For instance, the number density, and volume fraction of the nanoprecipitates decrease

while the diameter of the precipitates increases upon irradiation. However, the sink strength of the nanoprecipitates in the irradiated region of NiCoFeCrCu_{0.12} is estimated to be $7.1 \times 10^{15} / \text{m}^2$, remaining comparable to high swelling-resistant ODS⁶⁸. These analyses show that Cu-rich nanoprecipitates with a stable, coherent interface act as recombination centers for irradiation-induced vacancies and interstitials.

Our DFT calculations estimated lower vacancy formation energy for Ni, Co, Fe, and Cr elements at the interfaces of the Cu-rich phase and NiCoFeCr phase, indicating that vacancies prefer to be present at the interface. Similar calculations on the stability of Ni interstitials at the Ni | Cu interface revealed interfaces to be more energetically favorable sites for interstitials than the bulk. This indicates that vacancies and interstitials are stable at the interfaces compared to bulk. Such point defect stability favors vacancy and interstitial recombination at the interfaces, which could explain the little swelling observed experimentally in NiCoFeCrCu_{0.12}.

Multicomponent single-phase alloys have been demonstrated to exhibit enhanced irradiation tolerance, such as resistance to swelling and hardening²⁴. For instance, NiCoFeCr and NiCoFeCrMn multicomponent alloys resist void swelling much more effectively than binary and ternary alloys with the same chemical constituents at elevated temperatures up to doses of ~50 dpa^{16, 18, 23}. Lu et al. showed using molecular dynamics (MD) simulations and irradiation experiments that reduced defect mobility and altered defect migration path – long-range one-

dimensional mode to short-range three-dimensional mode for interstitial clusters – arising from suitable chemical complexity to rationalize radiation tolerance in multicomponent alloys^{18, 24, 69}. However, at higher doses (>100 dpa) and similar temperatures, these multicomponent alloys have been found to suffer from enhanced void swelling and a significant increase in dislocation density upon irradiation²³. Such irradiation performance could disregard the multicomponent alloys as candidate materials for core structural components in advanced nuclear reactors. In this study, however, we demonstrate that the radiation tolerance of multicomponent alloys can be enhanced by incorporating a high density of defect recombination centers via nanoprecipitates. Further examination of the radiation behavior of NiCoFeCrCu_{0.12} up on co-implantation with gas atoms such as helium (dual beam irradiation) and neutron irradiation under a wider range of temperatures will expand our understanding of its radiation tolerance. Such studies will shed light on the effect of helium, a by-product of (n,α) transmutation reaction in fission and fusion reactors, on swelling and mechanical behavior of the Cu-added HEA.

We rationalize the extraordinary radiation tolerance of NiCoFeCrCu_{0.12} to a materials design strategy using synergistic effects of suitable chemical complexity and high-density coherent interfaces having high sink strength for effective defect recombination. Our swelling-resistant alloy with FCC crystal structure will likely bring in a host of other benefits, such as better creep resistance and lower ductile-brittle transition temperatures, which could be problematic in BCC-based alloys,

including ferritic steels^{6,70}. Such a design strategy can be extrapolated to, in principle, any multicomponent materials system by choosing a suitable alloy composition that would produce stable second phases with a high sink strength for altering defect energetics for favorable recombination. Furthermore, to improve their radiation tolerance, second-phase particles with a high sink strength can be added to high entropy alloy matrices, similar to the case of ODS steels.

CONCLUSIONS

We synthesized a NiCoFeCrCu_{0.12} HEA with an FCC structure and a high density of Cu-rich nan precipitates. We demonstrate using systematic experiments that the irradiation performance of NiCoFeCrCu_{0.12} in terms of void swelling and radiation-induced hardening is significantly better than NiCoFeCr under ion irradiations up to a dose of 500 dpa at 475–580 °C. We show that the void swelling resistance of NiCoFeCrCu_{0.12} stands markedly better than austenitic stainless steels. Notably, the void swelling resistance of NiCoFeCrCu_{0.12} is comparable to other well-known radiation-resistant alloys, such as oxide-dispersion strengthened steels and ferritic steels, even though our alloy has a face-centered cubic crystal structure that has typically shown pronounced radiation-induced swelling. Using advanced characterization tools such as transmission electron microscopy and atom probe tomography, we reveal that the sink strength of the nan precipitates remains high ($\sim 7 \times 10^{15} /m^2$) in the HEA up to irradiations of ~ 100 dpa. Furthermore, the nan precipitates maintained coherent interfaces with the matrix upon high-dose

irradiation. Our DFT calculations predict lower formation energies of vacancies and interstitials at Cu-rich nanoprecipitate interfaces. We conclude that the effective point defects recombination at the interface enables high radiation resistance based on the results. We propose extending this design strategy to other multicomponent-based material systems to develop high radiation-resistant alloys for advanced nuclear and propulsion concepts.

ASSOCIATED CONTENT

Supporting information

X-Ray diffraction patterns collected from the HEAs, TEM bright-field images showing radiation-produced void swelling at 580 °C, TEM bright-field images of Au ion irradiated NiCoFeCrCu_{0.12} up to 500 dpa, STEM-EDS maps showing Cu-rich nanoprecipitates in Au³⁺ irradiated NiCoFeCrCu_{0.12} up to 500 dpa, and STEM-EDS and APT maps of Ni²⁺ irradiated NiCoFeCr.

ACKNOWLEDGMENTS

This work was supported as part of the Energy Dissipation to Defect Evolution (EDDE), an Energy Frontier Research Center funded by the U.S. Department of Energy, Office of Science, Basic Energy Sciences under contract number DE-AC05-00OR22725. Ion irradiations were performed at the Ion Beam Materials Laboratory (IBML), located at the University of Tennessee, Knoxville campus. APT research was supported by the Center for Nanophase Materials Sciences (CNMS), a US Department of Energy Office of Science User Facility at Oak Ridge National Laboratory. The authors would like to thank James Burns for his assistance in performing APT sample preparation and running the APT experiments. High-resolution atomic imaging work was through the Laboratory Directed Research and Development

Program at Idaho National Laboratory under the Department of Energy (DOE) Idaho Operations Office (an agency of the U.S. Government) Contract DE-AC07-05ID145142. The authors would like to thank Jatuporn Burns for her assistance in performing TEM sample preparation for high-resolution imaging.

REFERENCES

- (1) Pravilie, R.; Bandoc, G. Nuclear energy: Between global electricity demand, worldwide decarbonisation imperativeness, and planetary environmental implications. *J Environ Manage* **2018**, *209*, 81-92. DOI: 10.1016/j.jenvman.2017.12.043.
- (2) Zinkle, S. J.; Was, G. S. Materials challenges in nuclear energy. *Acta Materialia* **2013**, *61* (3), 735-758. DOI: 10.1016/j.actamat.2012.11.004.
- (3) Kombaiah, B.; Edmondson, P. D.; Wang, Y.; Boatner, L. A.; Zhang, Y. Mechanisms of radiation-induced segregation around He bubbles in a Fe-Cr-Ni crystal. *Journal of Nuclear Materials* **2019**, *514*, 139-147. DOI: 10.1016/j.jnucmat.2018.11.030.
- (4) Garner, F. A. Radiation-Induced Damage in Austenitic Structural Steels Used in Nuclear Reactors. In *Comprehensive Nuclear Materials*, 2020; pp 57-168.
- (5) Zinkle, S. J.; Snead, L. L. Designing Radiation Resistance in Materials for Fusion Energy. *Annual Review of Materials Research* **2014**, *44* (1), 241-267. DOI: 10.1146/annurev-matsci-070813-113627.
- (6) Murty, K. L.; Charit, I. Structural materials for Gen-IV nuclear reactors: Challenges and opportunities. *Journal of Nuclear Materials* **2008**, *383* (1-2), 189-195. DOI: 10.1016/j.jnucmat.2008.08.044.
- (7) Garner, F. A.; Toloczko, M. B.; Sencer, B. H. Comparison of swelling and irradiation creep behavior of fcc-austenitic and bcc-ferritic/martensitic alloys at high neutron exposure. *Journal of Nuclear Materials* **2000**, *276* (1), 123-142. DOI: [https://doi.org/10.1016/S0022-3115\(99\)00225-1](https://doi.org/10.1016/S0022-3115(99)00225-1).
- (8) Sun, C.; Zheng, S.; Wei, C. C.; Wu, Y.; Shao, L.; Yang, Y.; Hartwig, K. T.; Maloy, S. A.; Zinkle, S. J.; Allen, T. R.; et al. Superior radiation-resistant nanoengineered austenitic 304L stainless steel for applications in extreme radiation environments. *Sci Rep* **2015**, *5*, 7801. DOI: 10.1038/srep07801.
- (9) Beyerlein, I. J.; Caro, A.; Demkowicz, M. J.; Mara, N. A.; Misra, A.; Uberuaga, B. P. Radiation damage tolerant nanomaterials. *Materials Today* **2013**, *16* (11), 443-449. DOI: 10.1016/j.mattod.2013.10.019.
- (10) Du, J.; Jiang, S.; Cao, P.; Xu, C.; Wu, Y.; Chen, H.; Fu, E.; Lu, Z. Superior radiation tolerance via reversible disordering-ordering transition of coherent superlattices. *Nat Mater* **2022**. DOI: 10.1038/s41563-022-01260-y.
- (11) Zhang, Y. Reassembled nanoprecipitates resisting radiation. *Nat Mater* **2022**. DOI: 10.1038/s41563-022-01283-5.
- (12) Kimoto, T.; Shiraishi, H. Void swelling and precipitation in a titanium-modified austenitic stainless steel under proton irradiation. *Journal of Nuclear Materials* **1985**, *132* (3), 266-276. DOI: [https://doi.org/10.1016/0022-3115\(85\)90371-X](https://doi.org/10.1016/0022-3115(85)90371-X).

- (13) Choudhury, S.; Aguiar, J. A.; Fluss, M. J.; Hsiung, L. L.; Misra, A.; Uberuaga, B. P. Non-uniform Solute Segregation at Semi-Coherent Metal/Oxide Interfaces. *Sci Rep* **2015**, *5*, 13086. DOI: 10.1038/srep13086.
- (14) Lan, J.; Yang, Y.; Li, X. Microstructure and microhardness of SiC nanoparticles reinforced magnesium composites fabricated by ultrasonic method. *Materials Science and Engineering: A* **2004**, *386* (1-2), 284-290.
- (15) Zeng, L. F.; Gao, R.; Xie, Z. M.; Miao, S.; Fang, Q. F.; Wang, X. P.; Zhang, T.; Liu, C. S. Development of interface-dominant bulk Cu/V nanolamellar composites by cross accumulative roll bonding. *Sci Rep* **2017**, *7*, 40742. DOI: 10.1038/srep40742.
- (16) Jin, K.; Lu, C.; Wang, L. M.; Qu, J.; Weber, W. J.; Zhang, Y.; Bei, H. Effects of compositional complexity on the ion-irradiation induced swelling and hardening in Ni-containing equiatomic alloys. *Scripta Materialia* **2016**, *119*, 65-70. DOI: 10.1016/j.scriptamat.2016.03.030.
- (17) Kumar, N. A. P. K.; Li, C.; Leonard, K. J.; Bei, H.; Zinkle, S. J. Microstructural stability and mechanical behavior of FeNiMnCr high entropy alloy under ion irradiation. *Acta Materialia* **2016**, *113*, 230-244. DOI: 10.1016/j.actamat.2016.05.007.
- (18) Lu, C.; Niu, L.; Chen, N.; Jin, K.; Yang, T.; Xiu, P.; Zhang, Y.; Gao, F.; Bei, H.; Shi, S.; et al. Enhancing radiation tolerance by controlling defect mobility and migration pathways in multicomponent single-phase alloys. *Nat Commun* **2016**, *7*, 13564. DOI: 10.1038/ncomms13564.
- (19) Zhang, Y.; Stocks, G. M.; Jin, K.; Lu, C.; Bei, H.; Sales, B. C.; Wang, L.; Béland, L. K.; Stoller, R. E.; Samolyuk, G. D.; et al. Influence of chemical disorder on energy dissipation and defect evolution in concentrated solid solution alloys. *Nat Commun* **2015**, *6*, 8736. DOI: 10.1038/ncomms9736.
- (20) Pickering, E. J.; Carruthers, A. W.; Barron, P. J.; Middleburgh, S. C.; Armstrong, D. E. J.; Gandy, A. S. High-Entropy Alloys for Advanced Nuclear Applications. *Entropy (Basel)* **2021**, *23* (1). DOI: 10.3390/e23010098.
- (21) El-Atwani, O.; Li, N.; Li, M.; Devaraj, A.; Baldwin, J. K. S.; Schneider, M. M.; Sobieraj, D.; Wróbel, J. S.; Nguyen-Manh, D.; Maloy, S. A.; et al. Outstanding radiation resistance of tungsten-based high-entropy alloys. *Science Advances* **2019**, *5* (3). DOI: doi:10.1126/sciadv.aav2002.
- (22) Fu, Y.; Li, J.; Luo, H.; Du, C.; Li, X. Recent advances on environmental corrosion behavior and mechanism of high-entropy alloys. *J Mater Sci Technol* **2021**, *80*, 217-233. DOI: 10.1016/j.jmst.2020.11.044.
- (23) Fan, Z.; Yang, T.-n.; Kombaiah, B.; Wang, X.; Edmondson, P. D.; Ossetsky, Y. N.; Jin, K.; Lu, C.; Bei, H.; Wang, L.; et al. From suppressed void growth to significant void swelling in NiCoFeCr complex concentrated solid-solution alloy. *Materialia* **2020**, *9*. DOI: 10.1016/j.mtla.2020.100603.
- (24) Zhang, Y.; Zhao, S.; Weber, W. J.; Nordlund, K.; Granberg, F.; Djurabekova, F. Atomic-level heterogeneity and defect dynamics in concentrated solid-solution alloys. *Current Opinion in Solid State and Materials Science* **2017**, *21* (5), 221-237. DOI: 10.1016/j.cossms.2017.02.002.
- (25) Zhang, Y.; Ossetsky, Y. N.; Weber, W. J. Tunable Chemical Disorder in Concentrated Alloys: Defect Physics and Radiation Performance. *Chem Rev* **2022**, *122* (1), 789-829. DOI: 10.1021/acs.chemrev.1c00387.
- (26) Kombaiah, B.; Jin, K.; Bei, H.; Edmondson, P. D.; Zhang, Y. Phase stability of single phase Al0.12CrNiFeCo high entropy alloy upon irradiation. *Materials & Design* **2018**, *160*, 1208-1216. DOI: 10.1016/j.matdes.2018.11.006.
- (27) Parkin, C.; Moorehead, M.; Elbakhshwan, M.; Zhang, X.; Xiu, P.; He, L.; Bachhav, M.; Sridharan, K.; Couet, A. Phase stability, mechanical properties, and ion irradiation effects in face-

- centered cubic CrFeMnNi compositionally complex solid-solution alloys at high temperatures. *Journal of Nuclear Materials* **2022**, *565*. DOI: 10.1016/j.jnucmat.2022.153733.
- (28) Chen, D.; Zhao, S.; Sun, J.; Tai, P.; Sheng, Y.; Yeli, G.; Zhao, Y.; Liu, S.; Lin, W.; Kai, W.; et al. Effects of minor alloying addition on He bubble formation in the irradiated FeCoNiCr-based high-entropy alloys. *Journal of Nuclear Materials* **2020**, *542*, 152458. DOI: <https://doi.org/10.1016/j.jnucmat.2020.152458>.
- (29) He, J. Y.; Wang, H.; Huang, H. L.; Xu, X. D.; Chen, M. W.; Wu, Y.; Liu, X. J.; Nieh, T. G.; An, K.; Lu, Z. P. A precipitation-hardened high-entropy alloy with outstanding tensile properties. *Acta Materialia* **2016**, *102*, 187-196. DOI: 10.1016/j.actamat.2015.08.076.
- (30) Cao, B.; Yang, T.; Liu, W.-h.; Liu, C. T. Precipitation-hardened high-entropy alloys for high-temperature applications: A critical review. *MRS Bulletin* **2019**, *44* (11), 854-859. DOI: 10.1557/mrs.2019.255.
- (31) Yang, Y.; Chen, T.; Tan, L.; Poplawsky, J. D.; An, K.; Wang, Y.; Samolyuk, G. D.; Littrell, K.; Lupini, A. R.; Borisevich, A.; et al. Bifunctional nanoprecipitates strengthen and ductilize a medium-entropy alloy. *Nature* **2021**, *595* (7866), 245-249. DOI: 10.1038/s41586-021-03607-y.
- (32) Liang, Y. J.; Wang, L.; Wen, Y.; Cheng, B.; Wu, Q.; Cao, T.; Xiao, Q.; Xue, Y.; Sha, G.; Wang, Y.; et al. High-content ductile coherent nanoprecipitates achieve ultrastrong high-entropy alloys. *Nat Commun* **2018**, *9* (1), 4063. DOI: 10.1038/s41467-018-06600-8.
- (33) Yang, T.; Zhao, Y. L.; Tong, Y.; Jiao, Z. B.; Wei, J.; Cai, J. X.; Han, X. D.; Chen, D.; Hu, A.; Kai, J. J.; et al. Multicomponent intermetallic nanoparticles and superb mechanical behaviors of complex alloys. *Science* **2018**, *362* (6417), 933-937. DOI: doi:10.1126/science.aas8815.
- (34) Zhang, X.; Hattar, K.; Chen, Y.; Shao, L.; Li, J.; Sun, C.; Yu, K.; Li, N.; Taheri, M. L.; Wang, H.; et al. Radiation damage in nanostructured materials. *Progress in Materials Science* **2018**. DOI: 10.1016/j.pmatsci.2018.03.002.
- (35) Han, W.; Demkowicz, M. J.; Mara, N. A.; Fu, E.; Sinha, S.; Rollett, A. D.; Wang, Y.; Carpenter, J. S.; Beyerlein, I. J.; Misra, A. Design of Radiation Tolerant Materials Via Interface Engineering. *Advanced Materials* **2013**, *25* (48), 6975-6979. DOI: 10.1002/adma.201303400.
- (36) Zhang, Y.; Crespillo, M. L.; Xue, H.; Jin, K.; Chen, C. H.; Fontana, C. L.; Graham, J. T.; Weber, W. J. New ion beam materials laboratory for materials modification and irradiation effects research. *Nuclear Instruments and Methods in Physics Research Section B: Beam Interactions with Materials and Atoms* **2014**, *338*, 19-30. DOI: 10.1016/j.nimb.2014.07.028.
- (37) Stoller, R. E.; Toloczko, M. B.; Was, G. S.; Certain, A. G.; Dwaraknath, S.; Garner, F. A. On the use of SRIM for computing radiation damage exposure. *Nuclear Instruments and Methods in Physics Research Section B: Beam Interactions with Materials and Atoms* **2013**, *310*, 75-80. DOI: 10.1016/j.nimb.2013.05.008.
- (38) Lorimer, G. W. Quantitative X-ray microanalysis of thin specimens in the transmission electron microscope; a review. *Mineralogical Magazine* **1987**, *51*, 49-60.
- (39) Thompson, K.; Lawrence, D.; Larson, D. J.; Olson, J. D.; Kelly, T. F.; Gorman, B. In situ site-specific specimen preparation for atom probe tomography. *Ultramicroscopy* **2007**, *107* (2), 131-139. DOI: <https://doi.org/10.1016/j.ultramic.2006.06.008>.
- (40) Oliver, W. C.; Pharr, G. M. An improved technique for determining hardness and elastic modulus using load and displacement sensing indentation experiments. *Journal of Materials Research* **1992**, *7* (6), 1564-1583. DOI: 10.1557/JMR.1992.1564 From Cambridge University Press Cambridge Core.
- (41) Zunger, A.; Wei, S.; Ferreira, L. G.; Bernard, J. E. Special quasirandom structures. *Phys Rev Lett* **1990**, *65* (3), 353-356. DOI: 10.1103/PhysRevLett.65.353.

- (42) Kresse, G.; Furthmüller, J. Efficiency of ab-initio total energy calculations for metals and semiconductors using a plane-wave basis set. *Computational Materials Science* **1996**, *6* (1), 15-50. DOI: [https://doi.org/10.1016/0927-0256\(96\)00008-0](https://doi.org/10.1016/0927-0256(96)00008-0).
- (43) Monkhorst, H. J.; Pack, J. D. Special points for Brillouin-zone integrations. *Physical Review B* **1976**, *13* (12), 5188-5192. DOI: 10.1103/PhysRevB.13.5188.
- (44) Methfessel, M.; Paxton, A. T. High-precision sampling for Brillouin-zone integration in metals. *Physical Review B* **1989**, *40* (6), 3616-3621. DOI: 10.1103/PhysRevB.40.3616.
- (45) Bachhav, M.; Robert Odette, G.; Marquis, E. A. α' precipitation in neutron-irradiated Fe-Cr alloys. *Scripta Materialia* **2014**, *74*, 48-51. DOI: 10.1016/j.scriptamat.2013.10.001.
- (46) Klueh, R. L.; Shingledecker, J. P.; Swindeman, R. W.; Hoelzer, D. T. Oxide dispersion-strengthened steels: A comparison of some commercial and experimental alloys. *Journal of Nuclear Materials* **2005**, *341* (2), 103-114. DOI: <https://doi.org/10.1016/j.jnucmat.2005.01.017>.
- (47) Wu, Z.; Gao, Y. F.; Bei, H. Single crystal plastic behavior of a single-phase, face-center-cubic-structured, equiatomic FeNiCrCo alloy. *Scripta Materialia* **2015**, *109*, 108-112. DOI: 10.1016/j.scriptamat.2015.07.031.
- (48) Chen, Y.; Fang, Q.; Liu, Y.; Liu, B.; Liu, Y.; Li, J.; Liaw, P. K. Void-shape dependent hardening model in irradiated face-centered-cubic metals. *Journal of Nuclear Materials* **2020**, *540*. DOI: 10.1016/j.jnucmat.2020.152281.
- (49) Hirst, C. A.; Granberg, F.; Kombaiah, B.; Cao, P.; Middlemas, S.; Kemp, R. S.; Li, J.; Nordlund, K.; Short, M. P. Revealing hidden defects through stored energy measurements of radiation damage. *Science Advances* **2022**, *8* (31), eabn2733. DOI: doi:10.1126/sciadv.abn2733.
- (50) Osetsky, Y. N.; Bacon, D. J. Atomic-scale mechanisms of void hardening in bcc and fcc metals. *Philosophical Magazine* **2010**, *90* (7-8), 945-961. DOI: 10.1080/14786430903164580.
- (51) Dennett, C. A.; So, K. P.; Kushima, A.; Buller, D. L.; Hattar, K.; Short, M. P. Detecting self-ion irradiation-induced void swelling in pure copper using transient grating spectroscopy. *Acta Materialia* **2018**, *145*, 496-503. DOI: 10.1016/j.actamat.2017.12.007.
- (52) Neustroev, V. S.; Garner, F. A. Severe embrittlement of neutron irradiated austenitic steels arising from high void swelling. *Journal of Nuclear Materials* **2009**, *386-388*, 157-160. DOI: <https://doi.org/10.1016/j.jnucmat.2008.12.077>.
- (53) Kupriyanova, Y. E.; Bryk, V. V.; Borodin, O. V.; Kalchenko, A. S.; Voyevodin, V. N.; Tolstolutskaya, G. D.; Garner, F. A. Use of double and triple-ion irradiation to study the influence of high levels of helium and hydrogen on void swelling of 8–12% Cr ferritic-martensitic steels. *Journal of Nuclear Materials* **2016**, *468*, 264-273. DOI: 10.1016/j.jnucmat.2015.07.012.
- (54) Chen, T.; Aydogan, E.; Gigax, J. G.; Chen, D.; Wang, J.; Wang, X.; Ukai, S.; Garner, F. A.; Shao, L. Microstructural changes and void swelling of a 12Cr ODS ferritic-martensitic alloy after high-dpa self-ion irradiation. *Journal of Nuclear Materials* **2015**, *467*, 42-49. DOI: 10.1016/j.jnucmat.2015.09.016.
- (55) Vatre, A.; Jourdan, T.; Ding, H.; Marinica, M. C.; Demkowicz, M. J. Non-random walk diffusion enhances the sink strength of semicoherent interfaces. *Nat Commun* **2016**, *7*, 10424. DOI: 10.1038/ncomms10424.
- (56) Wang, L.; Martin, D.; Chen, W.-Y.; Baldo, P. M.; Li, M.; Wirth, B. D.; Zinkle, S. J. Effect of sink strength on coherency loss of precipitates in dilute Cu-base alloys during in situ ion irradiation. *Acta Materialia* **2021**, *210*. DOI: 10.1016/j.actamat.2021.116812.
- (57) ZC, L.; Abe, H.; Ishikawa, M.; Sekimura, N. Effects of Ion Irradiation on Coherency of Precipitates in Cu-Co Alloy. *Materials transactions* **2005**, *46* (8), 1783-1785.

- (58) Woolhouse, G. R.; Ipohorski, M.; Mott, N. F. On the interaction between radiation damage and coherent precipitates. *Proceedings of the Royal Society of London. A. Mathematical and Physical Sciences* **1971**, *324* (1559), 415-431. DOI: doi:10.1098/rspa.1971.0147.
- (59) Knoll, R. W. *Effects of heavy-ion irradiation on the phase stability of several copper-base alloys*; Wisconsin Univ., Madison (USA), 1981.
- (60) Aidhy, D. S.; Lu, C.; Jin, K.; Bei, H.; Zhang, Y.; Wang, L.; Weber, W. J. Formation and growth of stacking fault tetrahedra in Ni via vacancy aggregation mechanism. *Scripta Materialia* **2016**, *114*, 137-141.
- (61) Kong, X. F.; Gao, N.; Beyerlein, I. J.; Yao, B. N.; Zheng, S. J.; Ma, X. L.; Legut, D.; Germann, T. C.; Zhang, H. J.; Zhang, R. F. Interface facilitated transformation of voids directly into stacking fault tetrahedra. *Acta Materialia* **2020**, *188*, 623-634. DOI: 10.1016/j.actamat.2020.02.044.
- (62) Suzuki, A.; Mishin, Y. Interaction of point defects with grain boundaries in fcc metals. *Interface Science* **2003**, *11* (4), 425-437.
- (63) Navale, S. S.; Demkowicz, M. J. Vacancy and interstitial interactions with crystal/amorphous, metal/covalent interfaces. *Journal of Nuclear Materials* **2020**, *539*, 152329.
- (64) Was, G. S. *Fundamentals of radiation Materials Science: Metals and Alloys* Springer, 2007.
- (65) Mansur, L. K. Void swelling in metals and alloys under irradiation: an assessment of the theory. *Nuclear Technology* **1978**, *40* (1), 5-34.
- (66) Troparevsky, M. C.; Morris, J. R.; Kent, P. R.; Lupini, A. R.; Stocks, G. M. Criteria for predicting the formation of single-phase high-entropy alloys. *Physical Review X* **2015**, *5* (1), 011041.
- (67) Li, Z.; Qiao, D.; Xu, Y.; Zhou, E.; Yang, C.; Yuan, X.; Lu, Y.; Gu, J.-D.; Wolfgang, S.; Xu, D.; et al. Cu-bearing high-entropy alloys with excellent antiviral properties. *J Mater Sci Technol* **2021**, *84*, 59-64. DOI: 10.1016/j.jmst.2020.12.027 PubMed.
- (68) Massey, C. P.; Dryepondt, S. N.; Edmondson, P. D.; Frith, M. G.; Littrell, K. C.; Kini, A.; Gault, B.; Terrani, K. A.; Zinkle, S. J. Multiscale investigations of nanoprecipitate nucleation, growth, and coarsening in annealed low-Cr oxide dispersion strengthened FeCrAl powder. *Acta Materialia* **2019**, *166*, 1-17. DOI: 10.1016/j.actamat.2018.11.062.
- (69) Aidhy, D. S.; Lu, C.; Jin, K.; Bei, H.; Zhang, Y.; Wang, L.; Weber, W. J. Point defect evolution in Ni, NiFe and NiCr alloys from atomistic simulations and irradiation experiments. *Acta Materialia* **2015**, *99*, 69-76. DOI: 10.1016/j.actamat.2015.08.007.
- (70) Chernov, V. M.; Kardashev, B. K.; Moroz, K. A. Low-temperature embrittlement and fracture of metals with different crystal lattices – Dislocation mechanisms. *Nuclear Materials and Energy* **2016**, *9*, 496-501. DOI: 10.1016/j.nme.2016.02.002.

TABLE OF CONTENTS

